Supplementary Materials

for

A numerical platform for predicting the performance of paper-based analytical devices

Lawrence K.Q. Yan, Sze Kee Tam, Ka Ming Ng

Dept. of Chemical and Biological Engineering
The Hong Kong University of Science and Technology
Clear Water Bay, Hong Kong

A manuscript submitted to *Analytical Methods*
Original submission: May 2024

Modified workflow for extracting the required van Genuchten parameters:

When solving the Richard's equation (Eq.(1)), the van Genuchten functions (Eqs. (4)&(5)) are used to iteratively solve for the pressure. With these functions, a pressure is mapped with a corresponding partial saturation; and a partial saturation is mapped with a corresponding relative permeability.

The parameters of the van Genuchten functions are obtained from fitting the functions on the water retention and relative permeability curve. A typical paper substrate has the water retention curve and relative permeability curve shown in the **Fig S1**.

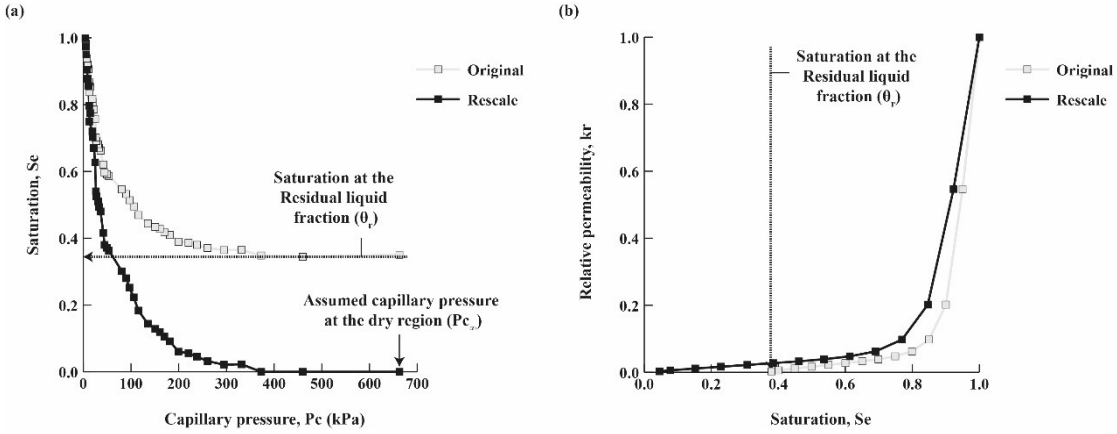

Fig S1: Common shapes of water retention (a) and relative permeability curve (b) of a paper substrate (Data extracted from Rath et. al. (2018)[1])

In the water retention curve **Fig S1a** , when the saturation goes below a certain threshold value, the pressure required to further reduce the saturation will approach infinity. Similarly, in the relative permeability curve, when the saturation goes below a certain threshold value, the relative permeability drops to about zero. Such threshold value is the saturation at the residual liquid fraction (θ_r)[2].

In previous reports[1,3,4], the van Genuchten functions' parameters are obtained by directly fitting the original curves and assuming a $\theta_r = 0$, possibly because of the paper device is oven-dry at the beginning of operation. With the set of fitted parameters obtained, the fluid flow is simulated by applying the dry region initial condition (Eq. (8)), using the largest capillary pressure obtained in the curve. With such implementation, previous reports accurately predicted the waterfront position at different time during the imbibition. However, because of the capillary pressure assumed is not the one at the saturation of 0, these simulations would have predicted an initial saturation (or water fraction) larger than 0 at the dry region. To deal

with this, Rath (2018 & 2021) [1,3] rescaled the saturation after the simulation during the post-processing, such that the prediction will have a saturation of 0 at dry regions.

When coupling with solute transport equation, such implementation will also underestimate the solute convection velocity. Rath (2021)[3] reported a predicted solute transport velocity of about 2x smaller in magnitude compared to the experimental results using such implementation. The reason behind that might attribute to the underestimation of the Darcy's velocity, a superficial velocity that is directly derived from the calculated pressure (Eq (2)) using such implementation. This in turns underestimates the convection of the solute in the solute transport equation when these equations are coupled.

The underestimation of the Darcy's velocity is a result of the shrunken space in the simulated porous volume due to the assumed initial water fraction. Using the above implementation, the initial water fraction is assumed as an inert volume when calculating the waterfront position; however, these volumes are still accountable when the Darcy's law is derived from the pressure calculated, and so does the convection velocity of solute, leading to a predicted value slower than the actual ones.

In this report, the parameters are fitted following the procedure suggested in Rudiyanto (2020)[5]. By first identifying the residual water fraction and the corresponding saturation, and rescaling both the water retention and relative permeability curves such that the maximum achievable pressure is located at saturation = 0. Afterwards, the van Genuchten functions' parameters are extracted from fitting the curves, while simultaneously minimizing the difference in the predicted and experimental waterfront position at different timepoints, of a straight rectangular strip. The parameters obtained are then used in simulating the fluid and solute transport. A similar workflow was also used in Liu(2019)[6] for coupling solute movement in underground waterflow in soil.

Implementation of case study 1: A colorimetric distance-based enzymatic sensor

1. Parameters used in the case study:

Diffusivity of glucose	9.59E-10 m²/s
Diffusivity of hydrogen peroxide	1.5E-9 m²/s
Diffusivity of the immobilized dye	0 m²/s
Diffusivity of the signal reporting molecule	0 m²/s
van Genuchten parameter: n	1.69
van Genuchten parameter: α	0.97
van Genuchten parameter: l	0.5
Permeability (k_s)	1.7E-13 m²
Porosity/ saturated liquid fraction (θ_s)	0.536
Residual liquid fraction (θ_r)	0.0897
Capillary pressure (Pc)	-5E5 Pa
Storage coefficient (S)	0
Liquid density	1000kg/m³
Liquid dynamic viscosity	1e-3Pas
Remaining effective liquid saturation (Se_r)	0.067
Michaelis Menten kinetics parameters (k_{cat}): GOx	2003 1/s
Michaelis Menten kinetics parameters (K_M): GOx	6.2 mol/m³
Michaelis Menten kinetics parameters (k_{cat}): HRP	10.53 1/s
Michaelis Menten kinetics parameters (K_M): HRP	0.11 mol/m³
Initial concentration of glucose ($C_{0,\ glucose}$)	10 mol/m³
Initial concentration of HRP ($C_{0,\ HRP}$)	0.011 mol/m³
Initial concentration of HRP ($C_{0,\ GOx}$)	5.825E-5 mol/m³
Initial concentration of the dye ($C_{0,\ Dye}$)	10 mol/m³

Table S1: Input parameters for the case study 1

These parameters are obtained from literatures[1,4], online databases[7] and deduced from the original article[8]. The diffusivities used in this example are the effective diffusivities, encompassing both the mechanical dispersion and the diffusion term. A discussion of the impact of considering the mechanical dispersion term to the device performance is shown in the next section.

2. Geometry setting:

The device is modelled as a circular sample reservoir with a radius of 5mm connected with a rectangular signal channel with a width of 2mm and length 40.5 mm. The geometry of the simulated device is shown in Fig. S2.

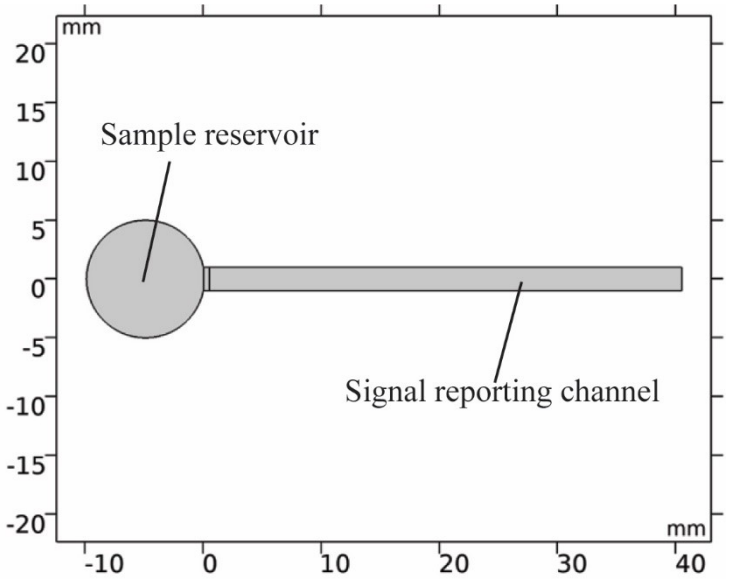

Fig. S2: Geometry of the simulated distance-based sensor

3. Study steps:

A single time-dependent step study is used to simulate the fluid imbibition from a saturated sample reservoir to an initially dry channel equation until the whole device is saturated. The simulation lasts for 15 minutes with results stored every 0.1 minute. A parametric sweep operation is added to the study step to perform the sensitivity analysis.

4. Imbibition modelling:

The imbibition is modelled by the Richard's equation with the following boundary and initial conditions:

- BC1: Pc=0 at all boundaries of the sample reservoir
- BC2: No slip conditions for all remaining boundaries.
- IC1: Pc = 0 at the domain of the sample reservoir.
- IC2: Pc = Pc_{∞} at the domain of the rectangular signal reporting channel

Note that as the Richard's equation is solved with the van Genuchten formulation, this will always result in a very small remaining saturation (Se_r) in the dry domain. This is because of the small inaccuracy of the curve fitting of the water retention curve at Se =0.

5. Solute transport

For the mobile solutes, the convection velocity is set as the same as the Darcy's velocity calculated from the imbibition model, and diffusion of solute in the fluid is modelled with the

diffusive term in the solute transport equation. For the immobilized solutes, both convection and diffusion terms are set as 0. As partial saturation of the liquid is considered, an "Unsaturated Porous Medium" is used for the solute transport models.

In the solute transport equation, the enzymatic reaction kinetics are modelled by Michaelis Menten kinetics.

The following boundary and initial conditions are used in solving the solute transport equations:

- BC1: $C_{glucose} = C_{0,\ glucose}$ at all boundaries of the sample reservoir.
- BC2: No flow conditions at the remaining boundaries.
- IC1: $C_{glucose} = C_{0,\ glucose}$ in the sample reservoir.
- IC2: $C_{mobile\ solute} = 0$ in the signal channel.
- IC3: $C_{immobilized\ solute} = C_{0,\ immobilized\ solute}/Se_r$ in the signal reporting channel where the solutes are immobilized. With this implementation. the immobilized components have higher effective concentration while the fluid saturation is low and will eventually become the set concentration once the device is saturated.

6. Mesh sequence:

   The mesh used in the simulation is shown in Fig. S3.

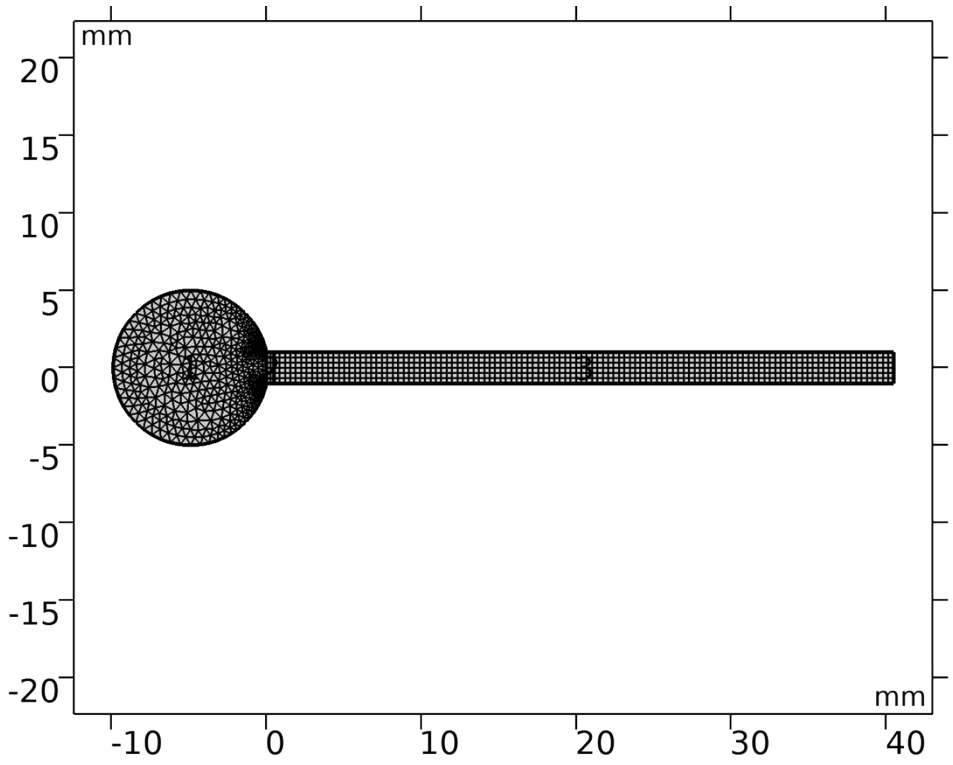

Fig. S3: Mesh generated with the mesh sequence.

Comparing the simulated device performance with and without the consideration of

In this section, we examined the effect of mechanical dispersion on the distance-based device performance. The effective diffusion is calculated using the formula of $D_\alpha = D_{0,\alpha} + sv_l$,[9] where D_α is the effective diffusivity in the fluid, s is the dispersity constant and v_l is the liquid convection velocity. As the dispersity constants for the chemical species in the selected porous medium are unavailable, a value of s of 30 um is used, which is obtained from the flow of a dye in a paper network[9]. The s is used in the diffusivities of all mobile species. The simulated performance of the distance-based sensor is shown in the Figure S4.

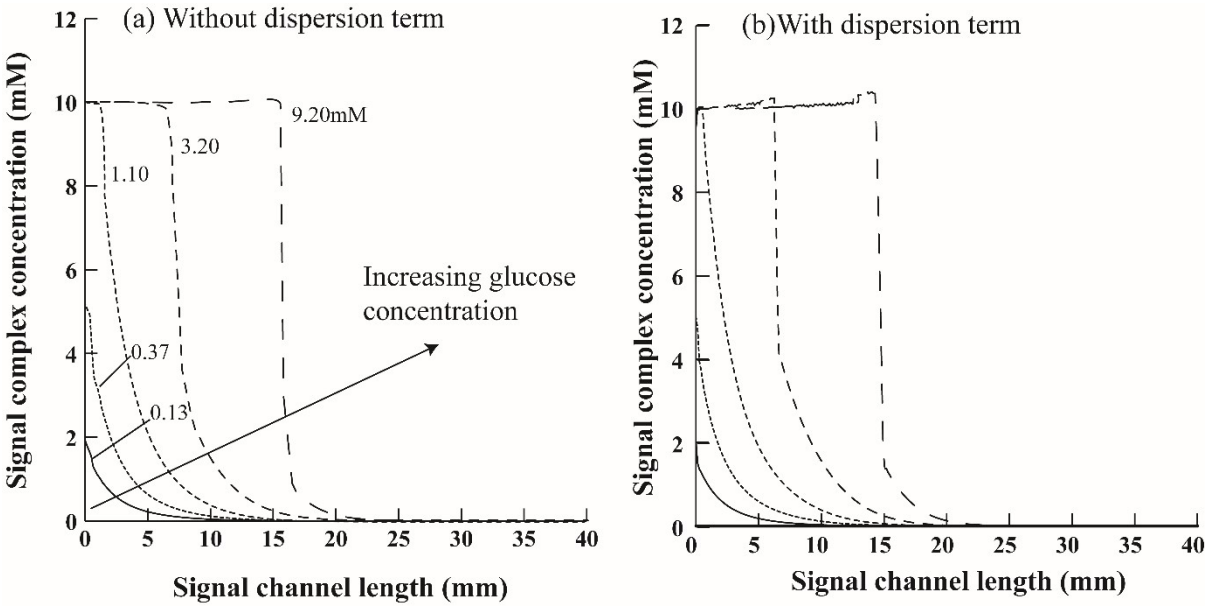

Fig. S4: The simulated signal complex concentration curves for different glucose concentrations (a) without and (b) with the consideration of the mechanical dispersion term.

From the Fig S4, it is observed including the mechanical dispersion does not impact much to the simulated device performance. This is probably because in devices driven by capillary force, the convection dominates the solute transport. This phenomenon is common in paper-based devices as evidenced by a similar result is also obtained from Rath(2021)[3], in which a Peclet number (Pe) of about 5000 is reported.

Implementation of case study 2: The amperometric detection of glucose

1. Parameters used in the case study:

Diffusivity of ferricyanide	7.3E-10 m²/s
Diffusivity of ferrocyanide	6.4E-10 m²/s
Diffusivity of glucose	9.59E-10 m²/s
Reference exchange current density ($i_{0,ref}$)	9.6485E7 A/m²
External electric potential	0.5 V
Boundary electric potential initial value of the counter electrode	0.1 V
Reference equilibrium potential	0 V
Anodic transfer coefficient (α_{an})	0.5
Liquid density	1000kg/m³
Liquid dynamic viscosity	1e-3Pas
van Genuchten parameter: n	2.564
van Genuchten parameter: α	0.1339
van Genuchten parameter: l	0.7654
Permeability (k_s)	9.4E-14 m²
Porosity/ saturated liquid fraction (θ_s)	0.75
Residual liquid fraction (θ_r)	0.064361
Capillary pressure (Pc)	-6.6297E5 Pa
Storage coefficient (S)	0
Michaelis Menten kinetics parameters (k_{cat}): GOx	2003 1/s
Michaelis Menten kinetics parameters (K_M): GOx	6.2 mol/m³
Initial glucose concentration ($C_{0,\ glucose}$)	22 mol/m³
Initial ferrocyanide concentration ($C_{0,\ ferro}$)	1 mol/m³
Initial Ferricyanide concentration ($C_{0,\ ferri}$)	600 mol/m³
Initial GOx concentration ($C_{0,\ GOx}$)	0.0208 mol/m³

Table S2: Input parameters for case study 2.

These parameters are obtained from the literature[1,4], online databases[7] and deduced from the original article[10].

2. Geometry setting:

The base-case device is modelled with a two-dimensional geometry, with a rectangular shape with a width of 24 mm and a height of 160μm. Four points are also added into the geometry to specify the boundary of the working and the counter electrode. The electrodes are 4mm in

width with a spacing of 1mm between them. The depth of the device is set as 4mm. The geometry of the simulated device is shown in Fig. S5.

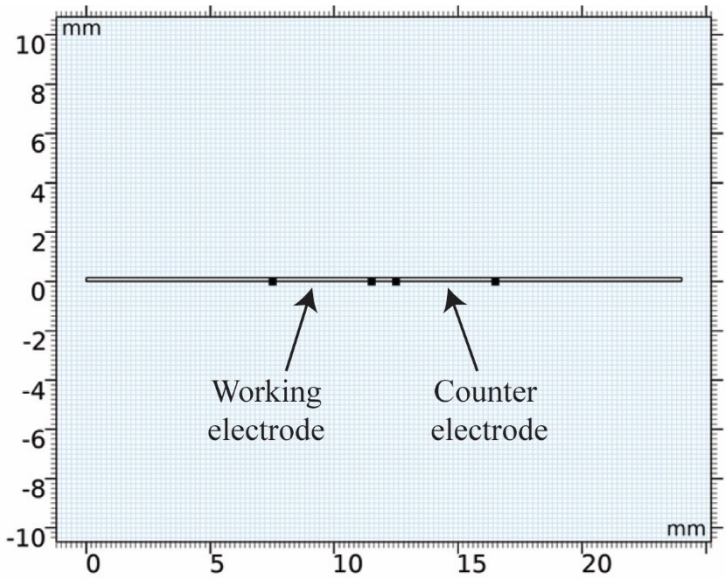

Fig. S5: Geometry of the simulated distance-based sensor

3. Study steps:

A single time-dependent step study is used to simulate the current signal measured from the device saturated with the sample glucose solution. The simulation lasts for 180 seconds with results stored every 0.01 second. A parametric sweep operation is added to the study step to perform the sensitivity analysis.

4. Imbibition modelling:

The imbibition is modelled by the Darcy's Law with the following boundary and initial conditions:

- BC1: Pc=0 at all boundaries of the device
- IC1: Pc = 0 at all domains of the device.

5. Solute transport

The enzymatic reaction kinetics are modelled using Michaelis Menten kinetics. The local current density is modelled using the Butler-Volmer kinetics with a reference exchange current density = $i_{0,ref}$ and an anodic transfer coefficient = α_{an}. The predicted current across the electrode surface is obtained by integrating the local current density on the working electrode surface.

The following boundary and initial conditions are used in the electroanalysis interface:

- BC1: Insulation at all boundaries
- BC2: No flow conditions at all boundaries.
- BC3: The boundary of the working electrode surface is set with an external electric potential of $\phi_{s,ext}$, with the equilibrium potential is expressed using the Nernst equation with the reference equilibrium potential = $E_{eq,ref}$.
- BC4: The boundary of the counter electrode surface is set with a boundary electric potential initial value of $\phi_{s,0}$. Other settings are similar to those for BC3.
- IC1: $C_{reagent} = C_{0,\ reagent}$ in the rectangular channel.

6. Mesh sequence:

   Due to the large number of elements and the high aspect ratio of the geometry, a portion of the generated mesh is shown in Fig. S6.

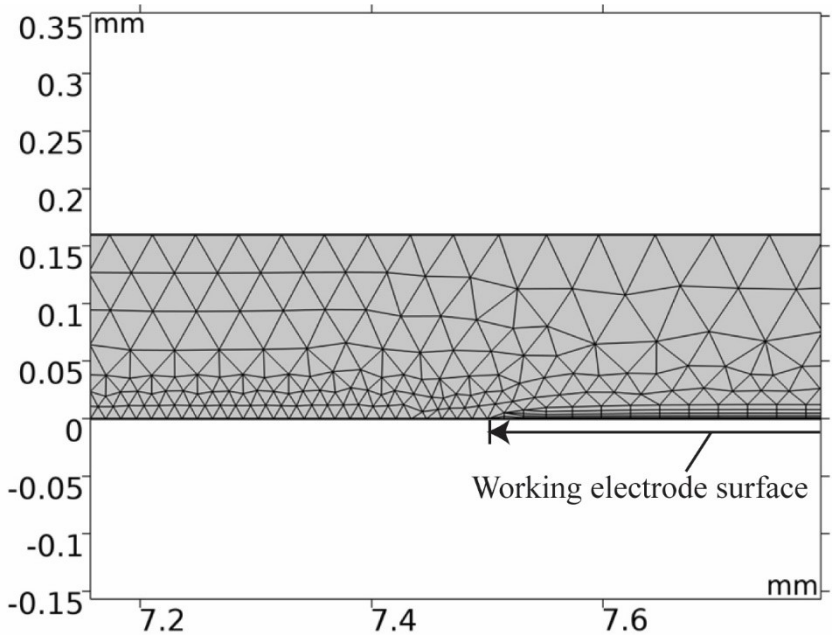

Fig. S6 A portion of the mesh generated.

Another example: Colloidal Gold-based, colorimetric Immunoassay enabled by automated sequential reagent addition

Immunoassay is another common assay type being used in $\mu PADs$ which employs the specific affinity of the antibodies to the antigens on the surface of the analyte molecules as the biorecognition mechanism. These assays are particularly suitable for examining protein analytes, such as proteins biomarkers found in various pathogenic infections. For example, colloidal gold-based immunoassays have been used as Rapid Antigen Tests (RATs) for quick diagnosis of COVID-19 during the pandemic.

The operation of the colloidal gold-based immunoassays requires sequential reagent addition and washing. The geometry of a common shape enabling this, and the configuration of the shape are shown in the (Fig. S7a &b) [11]. In such assays, the target analyte ***(A)*** solute carried in the sample fluid first reacts with some gold-conjugated antibodies ***(AuAb)*** (Fig.S7 ci)**.** Then, the resulting complexes ***(AAuAb)*** migrate (Fig.S7 cii) to the texting line where antibodies ***(AbT)*** targeting the analyte molecules are bound, forming a bound complex at the texting line (***AAuAbAbT)*** (Fig.S7 ciii). Besides the testing line, a control line is usually present to check the validity of the diagnosis, where antibodies ***(AbC)*** targeting the gold-conjugated antibodies are bound and will react when there are remaining (***AuAb)*** flow through the control line to form another bound complex. To remove any unbound antibodies, the lines are usually washed (Fig.S7 civ) after the reactions. And then, gold enhancement (***GE***) solution containing nano-gold particle will be carried to these lines and react with the bound complexes to form a larger gold aggregate at the lines and reporting darker colours (Fig.S7 cv).

Fig. S7 (a) Common geometry of pattern enabling sequential reagent delivery; (b) configuration of the colloidal gold immunoassay using the geometry; (c) the operating mechanisms of the colloidal gold immunoassay.

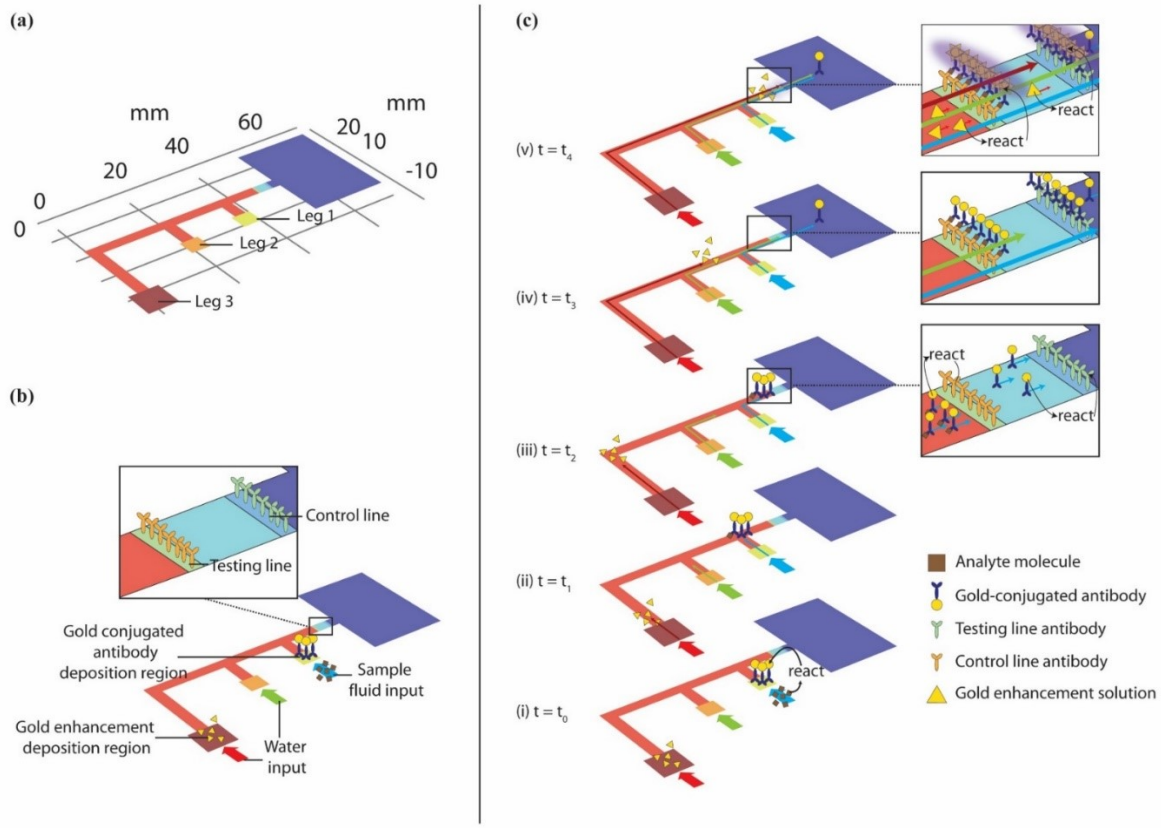

The water saturation and the chemical species concentration profiles are simulated and summarized at selected time in the (Fig.S8).

To clearly separate the fluid flow from each of the input legs to the testing and control lines, the fluid from each leg is traced with a virtual coloured particles moving in the same speed as the fluid (Fluid from Leg 1: Blue; Leg 2: Green; Leg 3: Red). The distribution of fluid from each leg at the selected time are summarized in the Fig.S8a. To accurately determine the arrival time of fluid from each leg, the concentration of these virtual particles are probed at the inlet boundary of the testing and control lines (Fig.S8 (b) and (c)), which shows that when all the three legs are immersed in infinite fluid sources, the fluid from Leg 1 will reach the testing and control line at 0.6 and 0.9 mins; the fluid from Leg 2 will reach these lines at 3.6 and 3.9 mins; while the fluid from Leg 3 will never reach the lines before the device is fully saturated.

The pattern of the reagent's movement and the concentration profile at the detection zone obtained from the simulation prediction are similar to the experimental data reported in Rath (2021)[3]. This indicates the capability of the simulation platform of predicting reagent-carrying flow in a more complicated pattern and with multiple fluid input sources.

The species concentration profiles are shown in the Fig.S8 (d) – (h). From these profiles, it is observed that both the gold-conjugated antibodies (Fig.S8(b)) and the gold-enhancement solution (Fig.S8 (g)) are capped at a concentration of 1000[uM], which is the assumed solubility of these molecules. The reaction between the target analyte molecule and the gold conjugated antibodies to form the complex is also correctly captured in the profile shown in the Fig.S8 (f); however a much higher concentration of the complex is recorded at the end of the assay, which is due to there is no constrain applied on the concentration of the complex (no solubility constrain is applied), and thus it will continue to accumulate in the simulated system. The concentration of the bound complexes is shown in the Fig.S8 (hi & ii). From the Figure, it is observed that the concentration of these species increases at the beginning (from 0 – 3.9 min) but drops a little bit later. While the increase in concentration is due to the correct capturing of the bound species with their corresponding mobile solute, the later decrease is due to the increase in liquid saturation afterward which dilutes the species at the bound region. From the Fig.S8 (hiii), it is observed that there is no signal generated, which is because no gold enhancement solution has reached the lines before

the device is completely saturated, which is also evidenced by the concentration profile of the gold enhancement solute in Fig.S8(g).

Fig. S8: Saturation and species concentration profiles at different selected time for the Example; (a) illustration of liquid flow from different fluid sources (Leg 1: Red; Leg 2: Green; Leg3: Blue); (b)& (c) the arrival time of fluid flow from the legs by tracing 100μM of virtual coloured particles carried in the legs (Blue: leg1; Green: Leg 2; Red: Leg 3) (the arrows indicate the time of the fluid from each of the legs arriving the testing (b) or control (c) line); concentration profile of the (d) analyte molecule; (e) gold-tagged antibodies; (f) analyte-gold-tagged antibody complexes; (g) gold enhancement particles; (h) concentration profile of the (i) complexes formed at the testing line; (ii) complexes formed at the control line; (iii) amplified signal from the reaction of the gold enhancement particles with the bound complexes

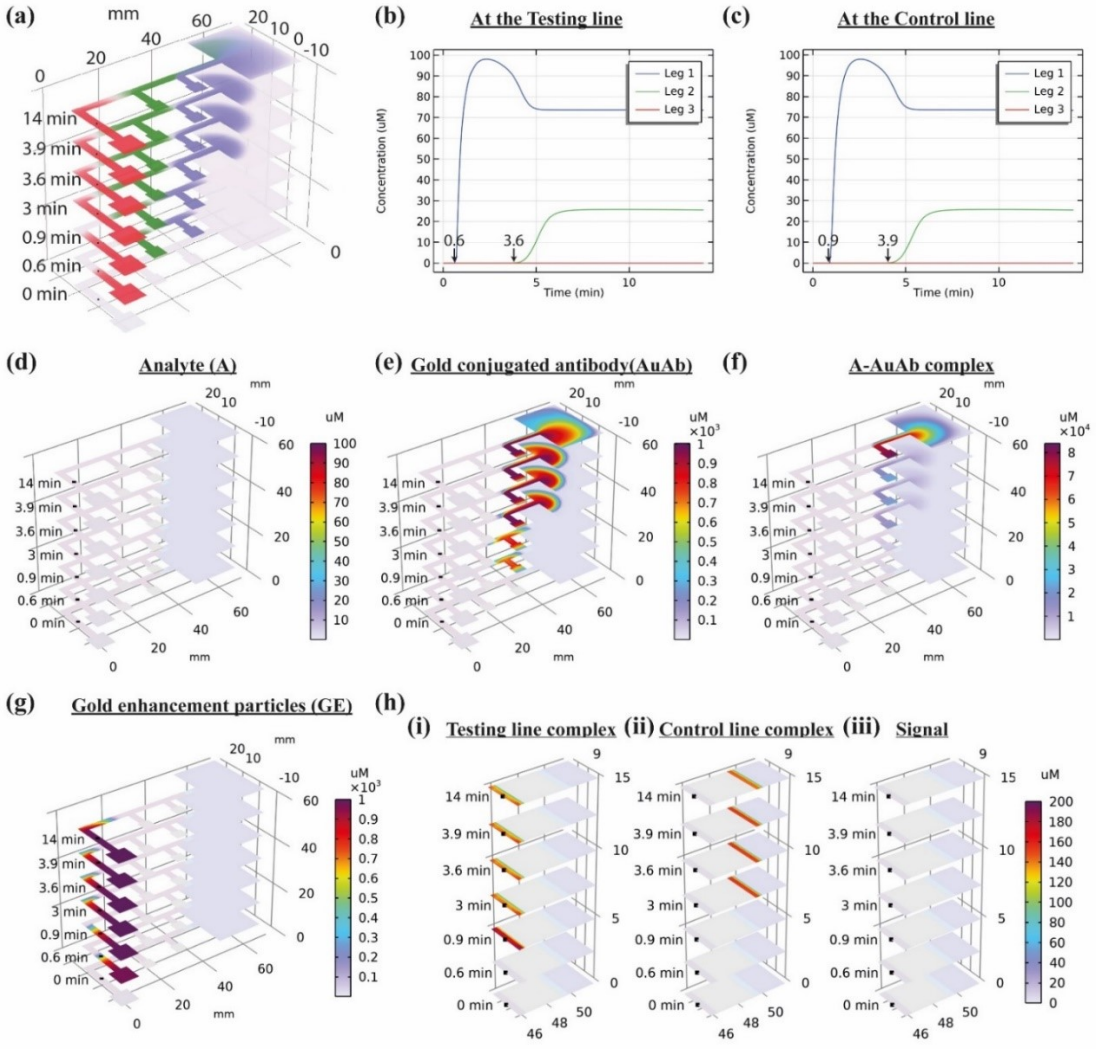

To improve the design and ensuring that the gold enhancement solution reaches the lines for giving an observable signal, a few strategies can be used. First, a larger waste zone can be used that increase the device's sample handling capacity, and thus prolonging the imbibition time and allow the fluid from the third leg reaches the line before it is completely saturated. Another method is to shorten the distance between the third leg and the lines. Yet still another strategy is to control the volume of the fluid input from the three legs. Since the fluid from the leg 1 is only needed at the very beginning of the assay to transport the analyte-gold conjugated antibody complexes and the excess antibodies to the lines, this can be stopped once it has reached the line to prevent the continuous fluid flow from leg 1 slowing down the arrival of fluid from the leg 3. Similar consideration can be made on fluid from the leg 2 as well. Seeing this, the volume of the fluid input from leg 1,2,3 is set at 10, 10 and 40μL.

The simulated results of the device operating in new fluid input scheme are summarized in the Fig S9 From the Fig S9(b) and (c), it is observed that when the fluid arrives the lines at about the same time as using the original fluid input scheme, the fluid from leg 2 arrives much slower. This is because the volume of the liquid from the leg 2 is not sufficient to reach the lines, and the fluid from leg 2 is indeed stopped at the middle of the fluid channel and is pushed by the fluid from leg 3 to the lines (Fig S9 (a): 1.1-5 min). This makes sequential delivery of fluid from the legs resembles the straight strip.

Fig. S9 Updated saturation and species concentration profiles at different selected time for the Example 3 with controlled fluid input volume in the three legs (10μL in Leg 1 and 2; 40μL in Leg 3); (a) illustration of liquid flow from different fluid sources (Leg 1: Red; Leg 2: Green; Leg3: Blue); (b)& (c) the arrival time of fluid flow from the legs by tracing 100μM of virtual coloured particles carried in the legs (Blue: leg1; Green: Leg 2; Red: Leg 3) (the arrows indicate the time of the fluid from each of the legs arriving the testing (b) or control (c) line); concentration profile of the (d) analyte molecule; (e) gold-tagged antibodies; (f) analyte-gold-tagged antibody complexes; (g) gold enhancement particles; (h) concentration profile of the (i) complexes formed at the testing line; (ii) complexes formed at the control line; (iii) amplified signal from the reaction of the gold enhancement particles with the bound complexes

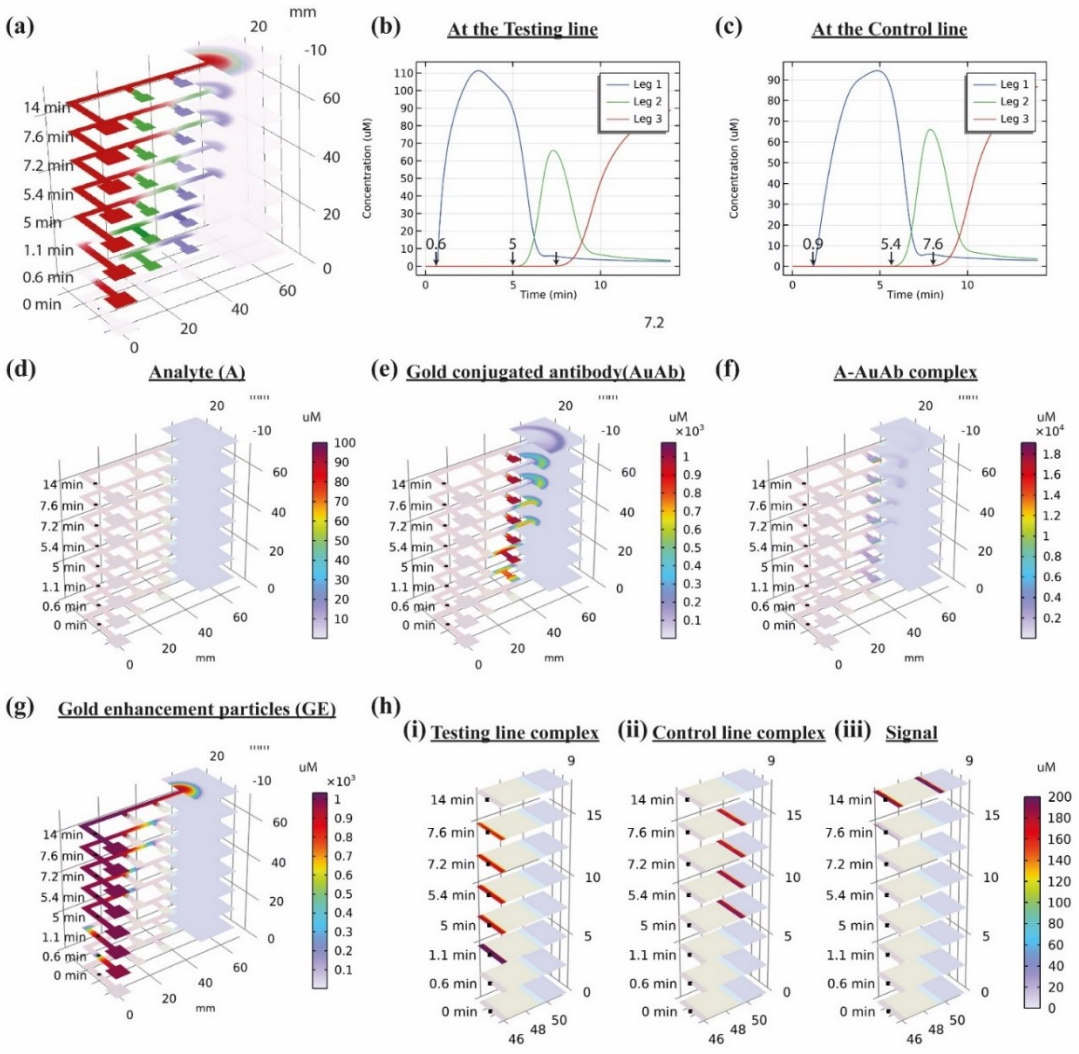
(a)
mm
14 min
7.6 min
7.2 min
5.4 min
5 min
1.1 min
0.6 min
0 min
(b) At the Testing line
Concentration (uM)
Time (min)
Leg 1
Leg 2
Leg 3
0.6
5
7.2
(c) At the Control line
Concentration (uM)
Time (min)
Leg 1
Leg 2
Leg 3
0.9
5.4
7.6
(d) Analyte (A)
uM
(e) Gold conjugated antibody(AuAb)
uM
×10³
(f) A-AuAb complex
uM
×10⁴
(g) Gold enhancement particles (GE)
uM
×10³
(h)
(i) Testing line complex
(ii) Control line complex
(iii) Signal
uM

configuration as reported by Dharmaraja (2013)[12], which has better and clear separation of fluids. This is also evidenced from the plots shown in the Fig S9 (b) and (c). Compared with the results obtained from the original scheme (Fig S9 (b) and (c)), the separation of fluids from different legs is cleaner, with the fluid from leg 1 almost completely drained off when the fluid from the second reaches the line; and the same when the fluid from the leg 3 replaces that from leg 2. With this scheme, the fluid from leg 3 has successfully reached the lines, and thus resulting in the successful reacting with the bound complexes at the lines and reporting the signal, which can be observed from the concentration profiles summarized in the Fig S9 (hi-iii). As the bound complexes at the lines having concentrations reduced to zero and converted to signal.

This example shows that the change in operating method, especially fluid input method, have important impact to the device performance and should be considered as a method of improving device performance. Apart from controlling the fluid volume, controlling the amount of deposited reagent (the gold conjugated antibodies/ the gold enhancement particles) can also be used as a strategy to make an even clearer separation of reagents from different fluid input in different legs, with a numerical implementation method similar to the control of fluid input volume. However, it is not included in this example for simplicity.

Reference

1. D. Rath, N. Sathishkumar, B.J. Toley, Langmuir, 2018, **34**, 8758–8766.
2. M. van Genuchten, Soil Sci Soc Am J., 1980,**44(5)**,892–898.
3. D. Rath, B.J. Toley, ACS Sensors, 2021, 6, 91–99.
4. R. Buser, S.A. Byrnes, C.E. Anderson, A.J. Howell, P.C. Kauffman, J.D. Bishop, M.H. Wheeler, S. Kumar, P. Yager, Analytical Methods, 2019, **11**, 336 - 345
5. Rudiyanto, B. Minasny, R.M. Shah, B.I. Setiawan, M.T. vanGenuchten, J Hydrol., 2020,**588**,125041.
6. K. Liu, G. Huang, X. Xu, Y. Xiong, Q. Huang, J. Šimůnek, Agric Water Manag. 2019,**213**,792–802.
7. SABIO-RK: Biochemical Reaction Kinetics Database.
8. D.M. Cate, W. Dungchai, J.C. Cunningham, J. Volckens, C.S. Henry, Lab Chip. 2013, **13**, 2397–2404.
9. R. Urteaga, E. Elizalde, C.L.A. Berli. Analyst. 2018;143,**10**,2259–2266.
10. Z. Nie, C.A. Nijhuis, J. Gong, X. Chen, A. Kumachev, A.W. Martinez, M. Narovlyansky, G.M. Whitesides, Lab Chip., 2010, **10**, 477–483.
11. E. Fu, T. Liang, P. Spicar-Mihalic, J. Houghtaling, S. Ramachandran, P. Yager, Anal Chem., 2012,**84(10)**,4574–4579.
12. S. Dharmaraja, L. Lafleur, S. Byrnes, Microfluid BioMEMS, Med Microsystems XI., 2013,**8615(206)**,86150X.